Heavily Doped poly(3,4-ethylenedioxythiophene) Thin Films with High Carrier Mobility Deposited Using Oxidative CVD: Conductivity Stability and Carrier Transport

*Sunghwan Lee, David C. Paine, and Karen K. Gleason**

The transparent conductingpoly(3,4-ethylenedioxythiophene) (PEDOT) is of interest for various optoelectronic device applications. Here, the conductivity stability of PEDOT processed using oxidative chemical-vapor-deposition (oCVD) with $FeCl_3$ as an oxidant is primarily dominated by the change in carrier density when aged in air. To establish the mechanism for the conductivity decrease, the changes in carrier density and carrier mobility of PEDOT films are separately monitored using an AC Hall Effect measurement system. The measured electrical properties reveal that a decrease in carrier density dominates the conductivity decrease during annealing. X-ray diffraction analysis made on the HBr- and MeOH-rinsed PEDOT samples identifies the Fe-related dedoping phase of $Fe(OH)_2$ and provides the dedoping mechanism. The carrier transport study demonstrates heavily doped oCVD PEDOT with the carrier density higher than ~10^{20} cm^{-3}, and in this regime, an increase in carrier density yields lower carrier mobility which shows that the carrier transport is governed by the ionized impurity scattering mechanism due to increased dopant counter-anions. These findings of the mechanisms for PEDOT conductivity decrease and carrier transport behavior may be important to organic optoelectronic device applications that show a strong effect of air-exposure and low-temperature annealing on the device stability and performance.

1. Introduction

High conductivity and excellent optical transparency in the visible regime (>80%) enables transparent conducting materials to be extensively used for a variety of optoelectronic device applications such as liquid crystal displays (LCD), organic light emitting diodes (OLED) and thin film solar cells. Of the commercially available transparent conducting materials, tin-doped In_2O_3 (ITO, typically 9.8 wt% SnO_2) is the most popular as a result of its well known reputation as the highest reported electrical conductivity (>5000 S cm^{-1}) and wide range of good optical transmittance (wavelength, $\lambda \approx$ 300–1300 nm). The use of ITO is limited by the high cost and limited supply of indium metal. Additionally ITO is brittle[1,2] and typically requires relatively high process temperature (≈350 °C)[3] to ensure crystalline-state highly conducting film, which is undesirable for the use of inexpensive and heat-sensitive polymer substrates in flexible device applications.[1–3] Efforts[4,5] to integrate ITO on flexible substrates have been made by utilizing low process temperature. However, low-temperature ITO on flexible polymer substrates (e.g., PET) resulted in significantly low ITO conductivity and, consequently, inferior OPV device efficiency compared to those using high-temperature deposited ITO.[4] It is also reported that cracks are developed during the bending tests and propagated through the entire ITO films on PET polymer substrates,[2] and the conductivity decreases with increasing tensile strength.[2] Currently, several transparent conducting materials are being explored as potential replacements for ITO: indium-free transition metal oxides, such as ZnO doped with Al[6,7] or Ga[6]; carbon-based materials, such as graphene[8] and carbon nanotubes[9,10]; and conducting polymers, for example polyacetylene[11] and poly(3,4-ethylenedioxythiophene) (PEDOT)[12] which are attractive for their abundance and mechanical flexibility which would enable low cost roll-to-roll manufacturing. Among these materials, conducting polymers based on PEDOT have received extra attention for potential use as hole transport layers and transparent electrodes (anode) in organic photovoltaic (OPV) applications for its ability to be deposited at lower temperature (RT: 150 °C) in addition to high conductivity (> ≈500 S cm^{-1}) and optical transparency (>85% in the visible regime).

Oxidative chemical vapor deposition (oCVD) PEDOT offers significant improvements in process and performance over conventional solution-based PEDOT:PSS. High purity gas phase process enables oCVD PEDOT to have the absence of dewetting defects causing non-uniformity in surface roughness and conductivity, and inherently conformal coating for the patterned substrates compared to liquid phase-processed PEDOT:PSS.

Dr. S. Lee, Prof. K. K. Gleason
Department of Chemical Engineering
Massachusetts Institute of Technology
Cambridge, MA 02139, USA
E-mail: kkg@mit.edu
Prof. D. C. Paine
School of Engineering
Brown University
Providence, RI 02906, USA

DOI: 10.1002/adfm.201401282

These advantages make oCVD PEDOT suitable for large area, flexible and transparent devices on polymer and even paper substrates. Previous researchers reported[12,13] the electrical conductivity and structural properties of oCVD PEDOT. Also top- and bottom-illuminated OPV devices were demonstrated[14] using oCVD PEDOT electrodes on various substrates including papers which show the power conversion efficiency of ≈2–3%.

Achieving stable conductivity over time after low temperature annealing in air is the next challenge for the implementation of PEDOT electrodes for OPV applications as unexpected decrease in conductivity of PEDOT films has been reported.[13,15–17] Huang et al.[18] reported that the electrical conductivity of PEDOT:PSS thin films becomes unstable after annealing in air by the rapid uptake of atmospheric moisture due to extremely hygroscopic nature of PEDOT:PSS. Kawano et al.[16] reported that the degraded efficiency of poly[2-methoxy-5-(3′,7′-dimethyloctyloxy)-1,4-phenylene vinylene] (MDMO-PPV)/[6,6]-phenyl C61-butyric acid methyl ester (PCBM) solar cell resulted from water absorption into the PEDOT:PSS used for hole transporting layer and, consequently, a decrease in conductivity of PEDOT when the device was exposed to water. It is also suggested[19] that post-heat treatment possibly shrinks the conductive regions which leads to a thermal degradation of PEDOT:PSS. Chelawat et al.[15] reported that the oCVD PEDOT films using $FeCl_3$ as a doping agent showed a significant decrease in conductivity during annealing in air at 100 °C and this conductivity instability was improved by the use of Br_2 gas as a dopant which was attributed to less volatility and a lower oxidation potential of bromine than chlorine. However, the use of Br_2 gas for the synthesis of PEDOT as a doping agent in vapor phase polymerization is limited due to its high toxicity.

Although the decreases in PEDOT conductivity reported in the literature[13,15–17] lead to significant degradation of OPV device performance, the mechanisms for the conductivity instability have hitherto not been fully understood. The present study sheds new light on these mechanisms. Small current AC Hall Effect measurements reveal that a significant decrease in carrier density is the primary factor contributing to the decrease in conductivity during annealing in air and X-ray diffraction (XRD) analysis clearly identifies, for the first time, the Fe-related dedoping phase of $Fe(OH)_2$ before and after the annealing process. These electrical and structural investigation allows to establish the dedoping mechanisms, which at least partially operate in vapor-polymerized PEDOT films with typical $FeCl_3$ oxidant to produce the $Fe(OH)_2$ dedoping phase. In addition, the carrier transport mechanism for the heavily doped PEDOT films and the 100% monomer dopability in oCVD system is also discussed. The findings regarding the mechanisms for the PEDOT conductivity decrease and carrier transport behavior are important for OPV-device stability studies that show the strong effects of air-exposure and low temperature annealing on OPV-device performance degradation.

2. Results

Since the PEDOT polymer in its undoped form is usually non-conductive or shows very little conductivity, oxidant is typically added as a doping agent to improve the conductivity of PEDOT. In vapor phase polymerization including oCVD, $FeCl_3$ which is solid phase with limited volatility is widely used due to its low sublimation temperature (≈100–300 °C), easier control than other liquid- or gas-phase agents, and ability to produce more uniform and denser film than that produced using other oxidants such as $CuCl_2$. Positive charges (holes) are introduced by $FeCl_3$ along the backbone structure of PEDOT as previously suggested[20] and these positive charges are balanced by the counter-anions ($FeCl_4^-$ or Cl^-) provided by the doping agent, $FeCl_3$.

Post-deposition rinsing has been shown to improve the electrical and physical properties of the vapor phase polymerized films, because as-processed conductive polymers are likely to contain a majority of residual oxidants and unreacted monomers on the surface and inside the film. These impurities are critically important as they decrease the electrical conductivity and they also act as scattering centers which are unfavorable to carrier transport. Methanol (MeOH) is typically employed to rinse the as-processed films to remove residual oxidants and monomers. However, this rinsing agent often fails to completely eliminate excess oxidants from the film. Since it is known that the low pH of the acidic solutions enhances the solubility of ferric materials and stability of the Fe-related compounds, in the present study, the conductivity stability is investigated on acid-rinsed and MeOH-rinsed oCVD PEDOT films, and the mechanisms for the conductivity instability are suggested. Among various acidic solutions such as HBr, HCl and H_2SO_4, HBr is selected to study due to bromine's low volatility[15] as well as the ability to dope PEDOT[21] additionally, which is of assistance to the enhancement of the electrical conductivity and stability. Of as-processed oCVD PEDOT films, half were rinsed with only MeOH and the other half were rinsed with 5 mol L^{-1} HBr acid followed by methanol rinse to wash out HBr. The electrical, structural and compositional characteristics of these two sets of samples were evaluated before, during and after annealing, and compared along with as-processed (unrinsed) samples.

Figure 1a presents photographs of the typical oCVD PEDOT films deposited on glass-slide substrates which were taken 5 hours after the deposition. Despite the fact that these films were deposited in the same run, a significant difference in film color was observed between unrinsed film (dark gray) and rinsed films (light blue). No macroscopic differences were seen in the two types (MeOH- and HBr-) of rinsed films. Unrinsed PEDOT film instantly begins to lose its transparency when exposed to the air and, in 5 h, the optical transmittance dropped to ≈48% due mainly to the oxidation of $FeCl_3$ on the surface and inside the unrinsed film. However, both MeOH- and HBr-rinsed films show no significant changes in their initial color and maintain high optical transmittance (> ≈85%) in 5 h and over several months. Figure 1b shows the AFM image of the as-deposited PEDOT film compared to those of the unannealed HBr- and MeOH-rinsed films. The rinsed films have significantly lower root mean square roughness (R_{rms}, 3.21 and 3.79 nm for HBr- and MeOH-rinsed samples, respectively) than ≈29.4 nm of unrinsed sample. This smoother morphology for rinsed films results from the removal of residual oxidants, reaction derivatives and unreacted monomers by rinsing. In particular, the $FeCl_3$ is susceptible to oxidation which can lead to dedoping; thereafter, the rinsing should contribute to improve

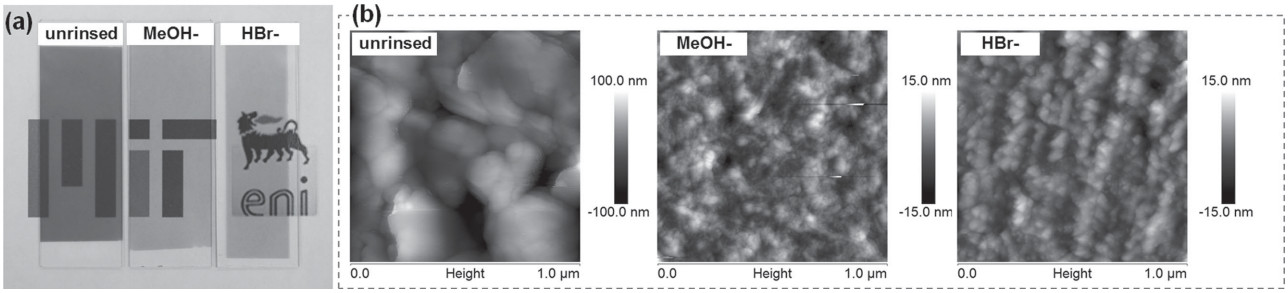

Figure 1. a) Photographs and b) AFM image images of the oCVD PEDOT films of the unrinsed, MeOH-rinsed and HBr-rinsed samples in as-deposited state, all deposited at the same run.

the stability of the conductivity over time, which is indeed observed in the electrical measurements during the annealing process. Note that between rinsed samples (Figure 1b), the AFM micro-image of the HBr-rinsed film shows better polymer alignment than that of MeOH-rinsed film.

To investigate the stability of PEDOT films, HBr- and MeOH-rinsed samples were annealed in air at temperatures of 45, 60, and 80 °C for more than 35 h. The anneal was only interrupted in order to record the change in sheet resistance (R_s) using a four point probe. The results are presented in **Figure 2**a and show that, while both HBr- and MeOH-rinsed samples show increases in sheet resistance at each temperature, the rate of change in sheet resistance is greatly enhanced for the MeOH-rinsed PEDOT films. The measured R_s shown on a single set of axes in Figure 2a clearly demonstrate that the rate of increase in R_s is thermally activated. A time constant (τ) for the increase in R_s was assigned for each temperature by selecting the time for the R_s to increase by 100% (or the initial conductivity to drop by 50%). The inverse of the characteristic time ($1/\tau$) provides a rate that is plotted on a conventional Arrhenius plot (Figure 2b) of rate ($1/\tau$) versus inverse absolute temperature. The activation energy for the R_s increase (i.e., conductivity decrease) was found to be 0.71 and 0.56 eV for HBr- and MeOH-rinsed samples from the Arrhenius plot, respectively. The lower activation energy in MeOH-rinsed samples indicates the kinetically faster rate of the decrease in conductivity than the rate in HBr-rinsed samples as shown in Figure 2a.

Since the conductivity (σ) is a function of both carrier concentration (p) and carrier mobility (μ) which is given by $\sigma = qp\mu$ (unit charge, $q = 1.6 \times 10^{-19}$ C) in p-type materials, a change in PEDOT conductivity depends on both parameters. To separately monitor the changes in carrier concentration and carrier mobility, and hence to mechanistically understand the conductivity decrease, Hall Effect measurements were made on the HBr- and MeOH-rinsed PEDOT films (≈50 nm-thick) during annealing in air at a temperature of 70 °C for 7 hours. The sheet resistance (**Figure 3**a) measured using Van der Pauw configuration presents the similar increase in sheet resistance shown in Figure 2a. The initial R_s is approximately 183.8 and 291.5 Ω sq^{-1} for HBr- and MeOH-rinsed samples, respectively and is increased during annealing to 311.8 and 674.2 Ω sq^{-1} in 7 h. These results reveal a significant increase in the rate of R_s change in MeOH-rinsed PEDOT film compared to HBr-rinsed film. Figure 3b shows corresponding changes in conductivity of both samples which can be understood from Hall measurements of the carrier density and carrier mobility taken during annealing. A plot of carrier density vs annealing time is shown in Figure 3c. The high initial carrier density of both HBr-rinsed (≈3×10^{21} cm^{-3}) and MeOH-rinsed (≈2×10^{21} cm^{-3}) samples in unannealed state indicates that these films are

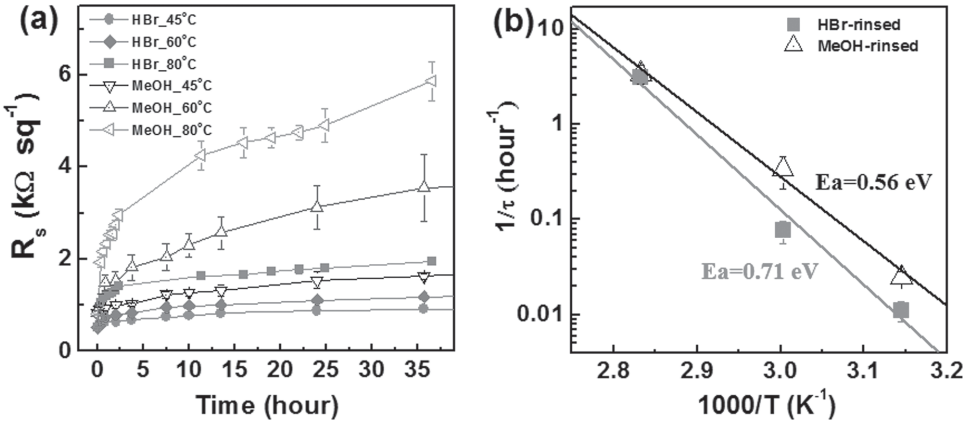

Figure 2. a) The change in sheet resistance of HBr- and MeOH-rinsed oCVD PEDOT films during annealing in air at temperatures of 45, 60, and 80 °C measured using a four-point probe. b) Arrhenius plot of $1/\tau$ vs reciprocal annealing temperature from which an activation energy for the conductivity decrease was found to be 0.71 eV and 0.56 ev for the HBr- and MeOH-rinsed PEDOT films, respectively.

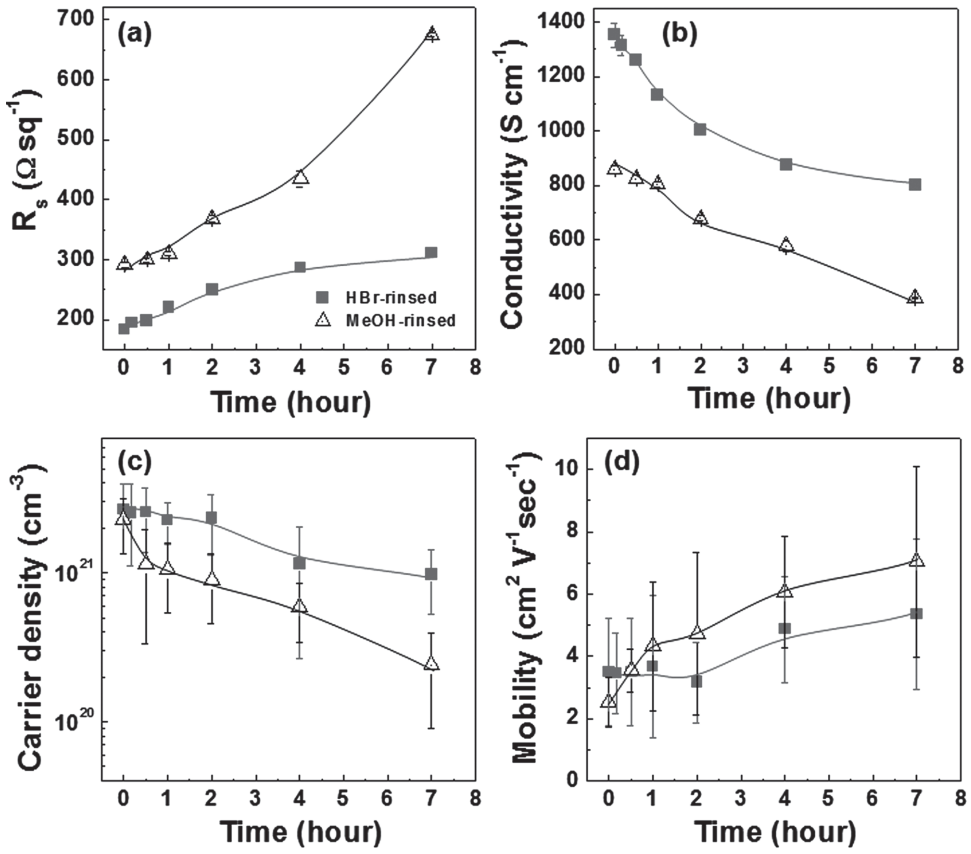

Figure 3. The changes in electrical properties of HBr- and MeOH-rinsed PEDOT during annealing in air at 70 °C using a small current AC Hall Effect measurement system via Van der Pauw configuration: change in a) sheet resistance, b) conductivity, c) carrier density, and d) carrier mobility.

degenerately doped; the Fermi level of both samples is located below the HOMO level which causes high conductivity in PEDOT films. The higher carrier density in HBr-rinsed film than that of MeOH-rinsed sample is achieved by the additional bromine doping during HBr rinsing.[21] However, upon annealing, the carrier density of the MeOH-rinsed sample decreases abruptly compared to the HBr-rinsed sample and, in 7 hours, drops by approximately an order of magnitude to ≈2.4 × 10^{20} cm^{-3}. On the other hand, the carrier density of the HBr-rinsed sample decreases to ≈9.8 × 10^{20} cm^{-3} which is significantly smaller change than that which occurred in the MeOH-rinsed PEDOT film.

The changes in carrier mobility (μ) with annealing time are presented in Figure 3d and show that the carrier mobility of the HBr-rinsed sample (≈4 cm^2 V^{-1} s^{-1}) is higher than that of the MeOH-rinsed sample (≈2 cm^2 V^{-1} s^{-1}) in unannealed state. Higher initial hole carrier mobility obtained in HBr-rinsed film is likely due to better polymer alignment compared to MeOH-rinsed sample in unannealed state as shown in the AFM image in Figure 1b. This is reversed as annealing begins; the MeOH-rinsed sample shows higher carrier mobility after annealing and at the end of the 7 h annealing process, carrier mobility for HBr-rinsed and MeOH-rinsed samples reach ≈5 and ≈8 cm^2 V^{-1} s^{-1} respectively.

Figure 4 shows Bragg-Brentano scan X-ray diffraction (XRD) spectra before and after air-annealing from the same HBr- and MeOH-rinsed PEDOT films used for Hall Effect

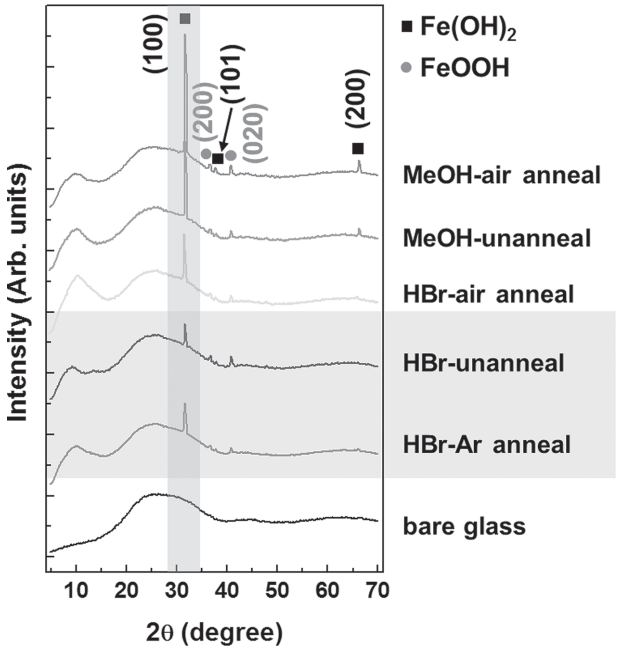

Figure 4. Bragg-Brentano X-ray diffraction patterns taken from the HBr- and MeOH-rinsed PEDOT films before and after air-annealing with the reference spectra of the Ar-annealed HBr-rinsed sample and bare glass substrate.

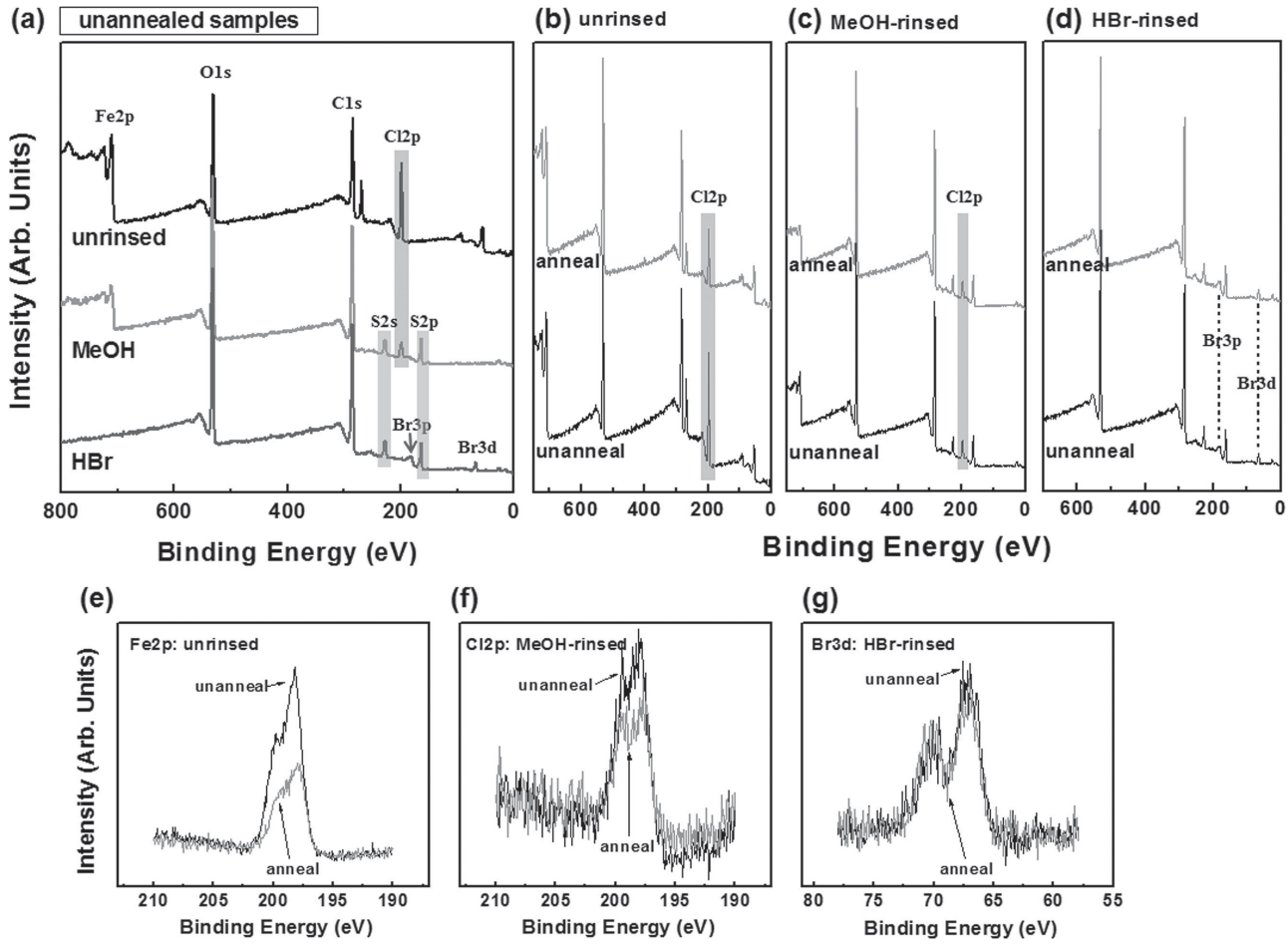

Figure 5. XPS survey scans: full spectra of the a) unannealed states of unrinsed, MeOH-rinsed, and HBr-rinsed PEDOT films, and the comparisons between unannealed and annealed states of b) unrinsed, c) MeOH-rinsed, and c) HBr-rinsed samples. High resolution spectra of the focused e) Cl 2p for unrinsed, f) Cl 2p for MeOH-rinsed, and g) Br 3d for HBr-rinsed films in unannealed and annealed states.

measurements. Diffraction patterns for the bare glass substrate and Ar-annealed HBr-rinsed sample are also included as references. Both the unannealed and annealed HBr-rinsed films show small intensity with their peaks of amorphous PEDOT at 2θ between ≈8–12°. However, after annealing the peak for amorphous PEDOT is slightly increased and shifted to the right. Another broad peak in the range of $15° < 2\theta < 35°$ is observed due to the glass substrate as shown in the reference spectra of the bare glass substrate. A sharp crystalline peak is also observed on the glass peak at 2θ of ≈31.7° which is determined to be $Fe(OH)_2$ (100) (from the JCPDS#00–013–0089) with crystalline $Fe(OH)_2$ (101) at $2\theta \approx 37.4°$. Crystalline peaks at 2θ of ≈36.5° and ≈40.8° were indexed as FeOOH (200) and (020), respectively (from the JCPDS#00–026–0792). Similarly, MeOH-rinsed samples show diffraction patterns of broad amorphous PEDOT and crystalline features of $Fe(OH)_2$ (100), (101), and FeOOH (200), (020) at the same 2θ detecting angles as in HBr-rinsed films. The additional crystalline peak at $2\theta \approx 66.2°$ is found to be $Fe(OH)_2$ (200), which was not detected in the HBr-rinsed samples. Note that the intensity of $Fe(OH)_2$ (100) peaks clearly increased after annealing in both HBr- and MeOH-rinsed films, and the intensity of the peaks of MeOH-rinsed films are significantly higher than those of HBr-rinsed films under both unannealed and annealed conditions. The diffraction pattern of the Ar-annealed HBr-rinsed sample is also obtained in order to compare air-annealed PEDOT films with the sample annealed in inert-gas ambient.

The reduction in $FeCl_3$ by rinsing was verified by X-ray photoemission spectroscopy (XPS). **Figure 5** presents the spectra obtained from the unrinsed, MeOH-rinsed and HBr-rinsed PEDOT films in both the unannealed and annealed states. Figure 5a compares an unrinsed film to rinsed samples in unannealed state. In the spectrum for unrinsed film, strong intensity is observed for both Fe 2p and Cl 2p, which is primarily attributed to a significant concentration of residual $FeCl_3$ and possibly to its reaction derivatives. The HBr-rinsed film shows no evidence of $FeCl_3$ (bottom plot in Figure 5a), while the MeOH-rinsed film clearly displays concentrations of Fe and Cl which are intermediate between those for the unrinsed and HBr-rinsed films. Hence, the XPS spectra shown in Figure 5a verify that HBr acid rinsing is a more efficient method to remove $FeCl_3$ residues than typical MeOH rinsing. Note that the XPS analysis is surface sensitive, typically probing only the uppermost ≈10 nm of film and photoelectrons are extracted only from a narrow solid angle.[22] In contrast, the XRD in typical Bragg-Brentano coupled scan mode is able to

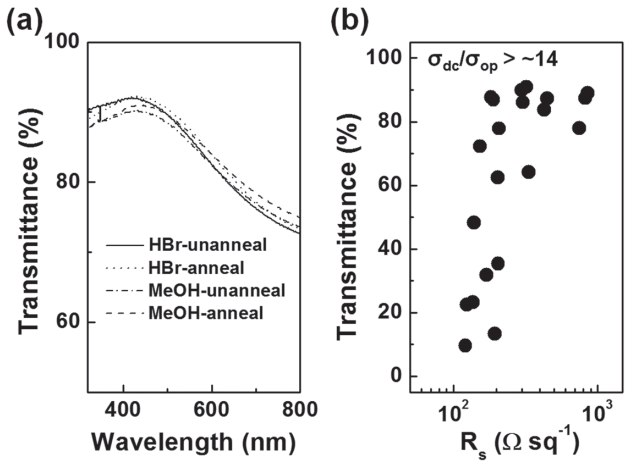

Figure 6. a) Optical transmission spectra in the visible regime wavelengths from 300 to 800 nm of HBr- and MeOH-rinsed samples in unannealed and annealed states, and b) dc and optical conductivity ratio (σ_{dc}/σ_{op}) which shows the trade-offs between optical transmittance (at 560 nm) and sheet resistance. oCVD PEDOT films in this study present σ_{dc}/σ_{op} of approximately 14.

evaluate the entire thickness of the films and shows Fe-containing crystallites even in the HBr- and MeOH-rinsed samples (Figure 4). Thus, the current rinsing process appears to be effective in the near surface region but not in the bulk of these ≈50 nm films. Longer rinsing times, higher rinsing temperatures, and the use of thinner films would all be expected to favor removal of residual oxidant from the entire thickness of the films. The XPS also reveals that dopant exchange process occurs with HBr rinsing. The Cl 2p peak is no longer detected in HBr-rinsed films and, instead, the characteristic peaks of Br 3p and Br 3d states are clearly seen at the binding energies of approximately 181 and 67 eV, respectively. When bromine acts as a dopant, a complex of the doped monomer unit ($EDOT^+$) and its counter-anion (Br^-) can be represented as [$EDOT^+Br^-$] and, therefore, a dopant exchange process is described by the equilibrium reaction:

$$H^+Br^- + EDOT^+Cl^- = H^+Cl^- + EDOT^+Br^- \quad (1)$$

This dopant exchange process through HBr acid rinsing contributes the improvement of the conductivity stability compared to the MeOH-rinsed PEDOT films due to the lower volatility and oxidation potential of bromine than chlorine. The XPS spectra of annealed samples are compared with unannealed films in **Figure 6**b–d of unrinsed, MeOH-, and HBr-rinsed oCVD PEDOT films respectively, and selected high resolution XPS spectra are shown in Figure 6e, f and g. All the Cl 2p core-level high resolution XPS spectra of unrinsed (Figure 6e) and MeOH-rinsed (Figure 6f) films before and after annealing show a spin-split doublet[12] of Cl $2p_{1/2}$ and Cl $2p_{3/2}$. After annealing, the intensity of the samples are decreased in both unrinsed and MeOH-rinsed PEDOT films which can account for the loss of chlorine. The Br 3d core-level high resolution spectra shown in Figure 6g are composed of two characteristic binding energies which include covalently bonded Br atoms (70.1 eV, C–Br bonds) and negatively charged Br^- species (67.9 eV).[23] The intensity of the Br 3d peak presents no significant change upon annealing due in part to bromine's lower volatility and oxidation potential compared to chlorine,[15] which is desirable for maintaining the high doping levels required for high film conductivity.

For the application of transparent electrodes, high optical transparency is also required while maintaining low sheet resistance. The optical transmission spectra for HBr- and MeOH-rinsed PEDOT films measured before and after annealing are shown in Figure 6a in the visible regime at wavelengths ranging from 300 to 800 nm. The UV–Vis spectra of all films (50 nm-thick) in this study present high transmittance greater than 85% at a wavelength (λ) of 560 nm and the transmission decreased as the wavelength increases due to an increase in light reflection and absorption. The optical transmission is slightly lower in MeOH-rinsed sample due to the absorption by the residual oxidant. However, no significant difference in optical transmission spectra is observed between unannealed and annealed states in both HBr- and MeOH-rinsed samples. A decrease in carrier density which decreases free carrier absorption may compensate for an increase of $Fe(OH)_2$ absorption after annealing. Figure 6b presents the plot of optical transmittance (at λ = 560 nm) versus sheet resistance of oCVD PEDOT films. The inverse relationship between optical transmittance and sheet resistance of oCVD PEDOT films is a typical example of trade-offs in transparent conductors, which results from an increase in free carrier absorption in high conducting films (i.e., low sheet resistance). In general, this relationship is explained by the ratio between the dc conductivity (σ_{dc}) and optical conductivity (σ_{op}) with the impedance of free space (Z_0 = 377 Ω):

$$T = \left(1 + \frac{Z_0}{2R_{sh}}\frac{\sigma_{op}}{\sigma_{dc}}\right)^{-2} \quad (2)$$

The ratio of oCVD PEDOT films, $\sigma_{dc}/\sigma_{op,}$ is as high as ≈14 which is comparable to previously reported PEDOT:PSS[24] thin films and carbon-based materials such as graphene,[25] graphene oxide[26] films and carbon nanotubes.[10,27] However, the current industrial standard for transparent conductor applications which is indium tin oxide (ITO) shows the σ_{dc}/σ_{op} of higher than ≈110 (when R_s = 20 Ω sq^{-1}, T = 85%) which is mainly due to its wide band gap (E_g) of approximately 4.0–4.8 eV[28] and this allows ITO to retain high transmittance with low enough sheet resistance. In contrast, the narrow band gap of PEDOT (≈1.5 eV[29] is responsible for the intrinsically higher absorption (i.e., lower transmittance) than wide band gap oxide transparent conductors (e.g., ITO). In the Beer-Lambert relation[30] of $A = \alpha l$, absorption (A) is a function of absorption coefficient (α) and path length (l). In general, the smaller band gap yields the larger absorption coefficient which increases light absorption.[31] Consequently, as the PEDOT film thickness increases, absorption significantly increases due to the effect of the relatively high absorption coefficient, and hence leads to low optical transmittance compared to ITO of the similar thickness. Further studies to improve the ratio between dc and optical conductivity are underway including efforts to achieve increased conductivity of PEDOT films by enhancing the carrier mobility through copolymerization to tailor the band gap and/or to cross-link the polymer chains.

3. Discussion

The results of Hall Effect measurements during annealing in air reveal that the decrease in PEDOT conductivity is primarily attributed to a decrease in carrier density since the effect of the increase in carrier mobility on the conductivity is much less than that of the decrease in carrier density in this study. A decrease in hole carrier density is likely due to dedoping by Fe in the counter-anions. A set of XRD spectra for both the HBr- and MeOH-rinsed films shown in Figure 4 clearly identifies the presence of $Fe(OH)_2$ in crystalline phase. A significant increase in peak intensity after annealing confirms the formation of $Fe(OH)_2$ during annealing process through Fe-related dedoping. Due to the presence of water (H_2O) and oxygen (O_2) in air, a type of counter-anion of $FeCl_4^-$ reacts with H_2O and O_2 via the reaction below:

$$FeCl_4^- + H_2O + \frac{1}{2}O_2 = Fe(OH)_2 + 2Cl_2 + e^- \quad (3)$$

where the formation of an $Fe(OH)_2$ liberates one electron, which was initially removed from PEDOT while leaving one *p*-type carrier (i.e., hole). The generated electrons reduce the hole carrier density in PEDOT by recombining with the holes and, consequently, decrease the electrical conductivity.

The difference in the $Fe(OH)_2$ (100) peak intensity between HBr- and MeOH-rinsed samples is possibly due to the $FeCl_3$ residue in MeOH-rinsed film. The residual $FeCl_3$ with H_2O and O_2 in air also form $Fe(OH)_2$ in a reaction:

$$FeCl_3 + H_2O + \frac{1}{2}O_2 = Fe(OH)_2 + \frac{3}{2}Cl_2 \quad (4)$$

where the formation of $Fe(OH)_2$ in reaction (3) accounts for much stronger diffraction intensity of the $Fe(OH)_2$ (100) peak in MeOH-rinsed films for both the unannealed and annealed states than those of HBr-rinsed samples. However, the reactions (2) and (3) do not provide sufficient explanation for the more rapid decrease in hole carrier density in MeOH-rinsed film shown in Figure 3c and the greater difference in XRD peak intensity (≈15 000 for MeOH-rinsed vs ≈8000 for HBr-rinsed counts) before and after annealing. Another dopant counter-anion in PEDOT of Cl^- may produce additional $FeCl_4^-$ when residual $FeCl_3$ exists. This transferred $FeCl_4^-$ along with H_2O and O_2 leads to reaction (2) forming additional $Fe(OH)_2$ via the reaction:

$$Cl^- + FeCl_3 = FeCl_4^- \xrightarrow{H_2O+\frac{1}{2}O_2} Fe(OH)_2 + 2Cl_2 + e^- \quad (5)$$

Consequently, in MeOH-rinsed samples, the large amount of residual $FeCl_3$ acts as a medium to form $Fe(OH)_2$ and reduce hole carrier density. This results in strong X-ray diffraction intensity for $Fe(OH)_2$ (100), and faster and greater decrease in carrier density-hence, conductivity-in the MeOH-rinsed sample. This excess drop in hole carrier density caused by residual $FeCl_3$ is responsible for the lower activation energy (0.56 eV vs 0.71 eV) for the conductivity decrease in the MeOH-rinsed sample shown in Figure 2. To verify that the suggested Fe-related dedoping mechanism is attributed to the presence of H_2O and O_2, an additional annealing experiment was conducted in Ar ambient on HBr-rinsed PEDOT film. In the XRD pattern shown in Figure 4 (2nd from the bottom), no significant changes were observed after Ar-annealing compared to un-annealed HBr sample, and consequently no significant conductivity decrease was expected in the films annealed in the inert ambient. By this inert gas-ambient annealing, it is confirmed that H_2O and O_2 play crucial roles in the Fe-related dedoping mechanism, hence the suggested reactions and mechanism may account, at least in part, for the conductivity instability of vapor deposited PEDOT films using typical $FeCl_3$ oxidant. Note that the generation of Cl_2 gas in the reaction (3), (4), and (5) is in accordance with the XPS results (Figure 5b,c,e,f) that describe the loss of Cl after annealing.

A similar conductivity instability was also reported for PEDOT:PSS.[18,32–34] These reports speculated that an observed decrease in electrical conductivity is primarily attributed to the effect of water during the annealing process. Since PEDOT:PSS is remarkably hygroscopic, the fast water uptake into the films arises from a thermal annealing in air.[18,34] A conductivity decrease by a disorder of polymer chain was reported in PEDOT[35] and PEDOT:PSS[33] as well. However, thus far, the conductivity degradation in PEDOT:PSS is not mechanistically understood.

An increase in carrier mobility for both the HBr- and MeOH-rinsed samples after annealing is observed and presented in Figure 3d. It is widely believed that the enhanced crystallinity of PEDOT improves the carrier mobility by the well-ordered polymer chain alignments. However, the XRD patterns in Figure 4 at $2\theta \approx 8$–$12°$ regime show no significant improvement in PEDOT crystallinity after annealing in both the HBr-rinsed and MeOH-rinsed films. Consequently, we concluded that the enhanced carrier mobility after annealing is not ascribed to the improvement of the PEDOT crystallinity.

The surface scattering is also a possible limiting factor of the carrier mobility. AFM surface topographic images of the annealed HBr- and MeOH-rinsed samples are shown in Figure 6a,b, respectively obtained using tapping height-mode. No significant topographic difference is observed between the HBr- and MeOH-rinsed samples. The root mean square roughness (R_{rms}) of the surface of the MeOH-rinsed sample (R_{rms} = 3.827 nm) is slightly higher than that of the HBr-rinsed sample (R_{rms} = 2.136 nm). Thus, the higher carrier mobility of the MeOH-rinsed film during and after annealing is not attributed to the differences in surface scattering or roughness between these samples. Instead, the change in carrier mobility can be understood to be an ionized impurity scattering occurring between charge carriers and counter-anions which is the mechanism by which heavy-doping limits the carrier mobility.

In **Figure 7**, a set of carrier mobility versus carrier density data for the HBr- and MeOH-rinsed PEDOT films from this study is plotted along with that for some other oCVD-deposited PEDOT samples. The contribution of ionized scattering centers using the Fermi-Dirac distribution function has been previously described by the following Brooks-Herring-Dingle (BHD) theory:[36]

$$\mu_I = \frac{24\pi^3(\varepsilon_0\varepsilon_r)^2\hbar^3 p}{e^3(m^*)^2 g(x)Z^2 n_I} \quad (6)$$

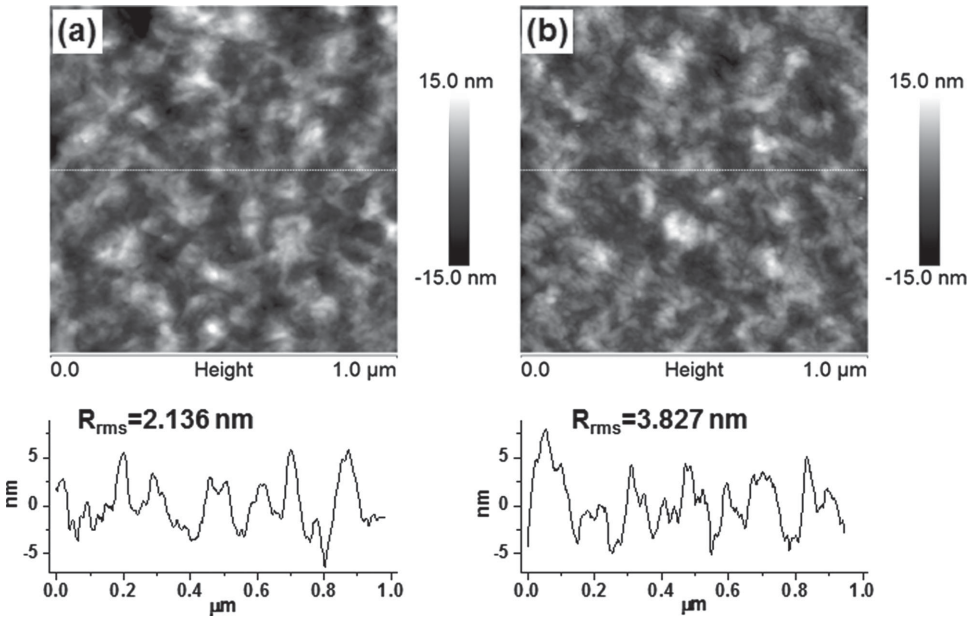

Figure 7. AFM topographic images of a) HBr-rinsed and b) MeOH-rinsed PEDOT films after annealing at the identical conditions used for the Hall Effect measurements in the scan area of 1 μm × 1 μm.

where μ_I is the mobility due to ionized charge centers, Z and n_I are the charge and density of the ionized scattering centers, respectively, and the scattering function $g(x)$ is defined as:

$$g(x) = \ln\left(1+\frac{4}{x}\right) - \left(\frac{1}{1+\frac{x}{4}}\right) \tag{7}$$

and

$$x = \frac{e^2(m^*)}{\pi\varepsilon_0\varepsilon_r\hbar^2\sqrt[3]{3\pi^5 p}} \tag{8}$$

Here, ε_0 and ε_r are the dielectric constant of free space and relative permittivity. m^* is the effective mass of the charge carriers. For these calculations, the values of $m^* = 0.121m_e$ and $\varepsilon_r = 5$ were taken from the literature.[37] The calculated μ_I due to the counter anions such as $FeCl_4^-$ and/or Cl^- using Equation 5 are plotted as a function of carrier density in **Figure 8**. The experimentally measured carrier mobility using the Hall Effect system is similar to the calculated μ_I with a slight deviation due possibly to the selected values (m^* and ε_r) for the calculation or other minor scatterings. Thus, the consistency between experimental Hall mobility and theoretical μ_I strongly supports the ionized impurity scattering mechanism that governs the carrier transport in the heavily doped PEDOT films.

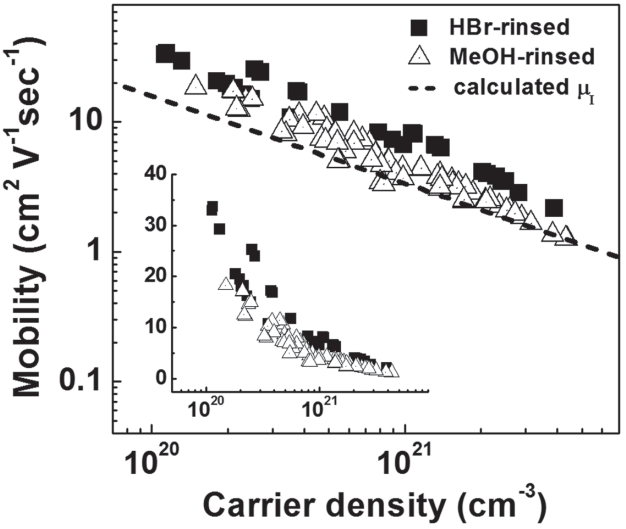

Figure 8. Carrier mobility (log scale) as a function of carrier density in HBr- and MeOH-rinsed PEDOT films. The calculated mobility (μ_I) (Equation (6) due to ionized charge centers is also shown by dotted line. At carrier density higher than ~10^{20} /cm^3, the mobility decreases with increasing carrier density which shows that the carrier transport is governed by the ionized impurity scattering. The inset shows the same data using a linear mobility scale.

In the same carrier density regime, the carrier mobility of HBr-rinsed samples is higher than that of MeOH-rinsed samples. The data plotted in Figure 8 show that in the carrier density regime higher than ~10^{20} cm^{-3}, an increase in carrier density leads to lower mobility possibly due to increased scattering by a large number of counter-anions such as Cl^- and $FeCl_4^-$. The maximum mobility for the HBr-rinsed sample was found, in this study, to be ≈33.6 cm^2 V^{-1} s^{-1} at a carrier density of ≈1.1 × 10^{20} cm^{-3}, and at a carrier density of ≈3.9 × 10^{21} cm^{-3}, the carrier mobility was measured as ≈2.27 cm^2 V^{-1} s^{-1}. We have concluded that an increase in hole carrier mobility after annealing is mainly attributed to a decrease in the effect of the ionized impurity scattering with decreasing counter-anions. The higher carrier mobility of the MeOH-rinsed sample than that of the HBr-rinsed sample after annealing is due to much lower carrier density (2.4 × 10^{20} vs 9.8 × 10^{20} cm^{-3}, respectively) in the film and hence, much less chance of the ionized scattering.

All PEDOT samples shown in Figure 8 are very heavily doped with the carrier density above ~10^{20} cm^{-3} for both HBr- and MeOH-rinsed samples. As a *p*-type semiconductor, the charge transport of PEDOT is solely contributed by holes. The maximum hole doping level can be estimated by the molecular weight of the monomeric unit of PEDOT (140 g mol^{-1}) and the density of oCVD PEDOT film which was determined to be approximately 1.3 g cm^{-3} using X-ray reflectivity. The density of EDOT monomer was obtained to be ≈5.6×10^{21} cm^{-3} from the above geometric consideration. Figure 7 shows that the maximum carrier density of our oCVD PEDOT films in this study reaches ≈4.8×10^{21} cm^{-3} which indicates that most of the EDOT monomers (≈90%) are doped by the counter anions. Note that this value is much higher than 1/3 of EDOT concentrations (≈1.9×10^{21} cm^{-3}) which is widely believed to be a hypothetical value of maximum hole density in PEDOT.[12,38] The previous assertion from the literature[12,38] may be based on the observation that further dopant incorporation results in little overall conductivity change, as the increase in carrier density is offset by a reduction in mobility.

4. Conclusions

We have separately monitored the changes in carrier density and carrier mobility before, during and after annealing in air to investigate the dominant parameter(s) for the conductivity decrease and, also, to establish the degradation mechanism. The AC Hall Effect electrical measurements show that the carrier density of PEDOT films decreases and the carrier mobility slightly increases with the decrease in conductivity during air annealing. This leads to a conclusion that a decrease in carrier density is a dominant factor for the conductivity instability rather than a change in carrier mobility. A decrease in conductivity of PEDOT with $FeCl_3$ oxidant is due to the formation of $Fe(OH)_2$ through the dedoping reaction by $FeCl_4^-$ in the presence of water and oxygen. This generates a negative charge that compensates for a positive charge in the PEDOT film and consequently, decreases the hole carrier density. This mechanism holds for both the HBr- and MeOH-rinsed PEDOT films. However, the lower activation energy for decreased conductivity in the MeOH-rinsed film suggests that an additional dedoping source may exist, thus reducing more carrier density via Cl^- reduction in the presence of the residual $FeCl_3$ in the film. Therefore, the MeOH-rinsed sample presents a more abrupt decrease in conductivity compared to the HBr-rinsed sample. These findings may lead to a significant implication about the conductivity stability of PEDOT polymer processed not only using oCVD method, but also using other solution- or vapor-phase polymerization that employs $FeCl_3$ as a doping agent.

The carrier transport studies reveal that heavily doped PEDOT with the carrier density higher than ~10^{20} cm^{-3} is dominated by the ionized impurity scattering. In this high carrier density regime, a large number of counter-anions limit the carrier mobility; an increase in carrier density leads to lower carrier mobility in PEDOT film. The maximum carrier density, in the present study, is as high as ≈5×10^{21} cm^{-3} (≈90% of monomers doped) which indicates that 100% monomer doping can be achieved with oCVD process with well-controlled process conditions.

5. Experimental Section

Preparation of oCVD PEDOT Films: The PEDOT films were synthesized and deposited by oCVD using commercially available 3,4-ethylenedioxythiophene (EDOT) monomer (Aldrich 97%) and $FeCl_3$ oxidant (Aldrich, 99.99%) without further purification. Glass substrates were cleaned with acetone, methanol and de-ionized water, and then fully blow dried substrates were loaded into the oCVD chamber. Before all depositions, the oCVD chamber was pumped down to a base pressure of less than 1×10^{-3} Torr. The initial rough vacuum (> ~10^{-2} Torr) was obtained by mechanical rotary pump and after reaching ~10^{-2} Torr, a molecular turbo pump was further employed to ensure the pressure below 1×10^{-3} Torr in the oCVD chamber. The depositions were performed at substrate temperature of 150 °C by simultaneously evaporating EDOT monomer at 140 °C and $FeCl_3$ oxidant from a crucible resistively heated at 160 °C. Half of as-deposited PEDOT films were rinsed with diluted (5 mol L^{-1}) hydrobromic acid (HBr, Aldrich 48%) for 20 min followed by methanol (MeOH) rinse for 20 mins. The other half were rinsed with only MeOH for 20 min immediately after deposition to investigate the effect of the rinsing solutions on the conductivity instability. For the rinsing process, samples were fully dipped into the rinsing liquid in the petri dish and were dried in the ambient. All rinsing and drying steps were performed in the hood. The HBr- and MeOH-rinsed films were annealed in air (relative humidity of ≈40%) at temperatures at 45, 60, 70, and 80 °C to investigate the activation energy and mechanism for the conductivity decrease at accelerated conductivity degradation conditions.

Characterizations: The electrical conductivity of oCVD PEDOT films were characterized before/after and during annealing in air using a four point probe (Jandel) and Hall Effect measurements system (custom setup[39]). The carrier concentration and the carrier mobility were also obtained using Hall Effect measurements with a 47.5 Hz small current source of ≈1 μA or less while the source current and the specimen voltage were recorded using lock-in amplifiers with input impedance of greater than 100 MΩ. A magnetic field of 5200 Gauss was used throughout measurements. Film thicknesses were measured using a step-height profilometer (Veeco Dektak 150). Bragg-Brentano X-ray diffraction analysis used to characterize amorphous/crystalline structure and preferred orientation of the materials was carried out in a PANalytical X'Pert Pro diffractometer with $3° < 2\theta < 70°$ using Cu $K\alpha$ radiation (λ = 1.54 nm) at 45 kV and 40 mA. X-ray photoelectron spectroscopy (XPS) measurements were performed under ultra high vacuum below 2×10^{-9} Torr using monochromatic Al Kα radiation at 1486.6 eV in a Surface Science Instruments SSX-100 spectrometer. Photoelectrons were collected at an angle of 55° from the surface normal. The surface topographic images and root mean square roughness were obtained using atomic force microscopy (AFM, Veeco Multimode) via non-contact height mode. Optical transmittance was measured using UV–Vis–NIR spectroscopy (Varian Cary 5000).

Acknowledgements

The authors gratefully acknowledge the financial support of the Eni S.p.A. under the Eni-MIT Alliance Solar Frontiers Program.

Received: April 21, 2014
Revised: July 25, 2014
Published online: September 10, 2014

[1] P. C. P. Bouten, P. J. Slikkerveer, Y. Leterrier, *Flexible Flat Panel Displays* **2005**, *99*.
[2] D. R. Cairns, R. P. Witte, D. K. Sparacin, S. M. Sachsman, D. C. Paine, G. P. Crawford, R. R. Newton, *Appl. Phys. Lett.* **2000**, *76*, 1425.
[3] B. Yaglioglu, Y. J. Huang, H. Y. Yeom, D. C. Paine, *Thin Solid Films* **2006**, *496*, 89.

[4] C. Lungenschmied, G. Dennler, H. Neugebauer, S. N. Sariciftci, M. Glatthaar, T. Meyer, A. Meyer, *Sol. Energy Mater. Sol. Cells* **2007**, *91*, 379.
[5] M. Al-Ibrahim, H. K. Roth, S. Sensfuss, *Appl. Phys. Lett.* **2004**, *85*, 1481.
[6] T. Minami, *MRS Bull.* **2000**, *25*, 38.
[7] a) S. Lee, S.-H. Kim, Y. Kim, A. I. Kingon, D. C. Paine, K. No, *Mater. Lett.* **2012**, *85*, 88; b) J. Hong, H. Paik, H. Hwang, S. Lee, A. J. deMello, K. No, *Phys. Status Solidi A* **2009**, *206*, 697.
[8] a) Y. Zhu, Z. Sun, Z. Yan, Z. Jin, J. M. Tour, *ACS Nano* **2011**, *5*, 6472; b) H. Park, R. M. Howden, M. C. Barr, V. Bulovic, K. Gleason, J. Kong, *ACS Nano* **2012**, *6*, 6370.
[9] L. B. Hu, D. S. Hecht, G. Gruner, *Chem. Rev.* **2010**, *110*, 5790.
[10] J. Li, L. Hu, L. Wang, Y. Zhou, G. Gruner, T. J. Marks, *Nano Lett.* **2006**, *6*, 2472.
[11] C. K. Chiang, C. R. Fincher, Jr., Y. W. Park, A. J. Heeger, H. Shirakawa, E. J. Louis, S. C. Gau, A. G. MacDiarmid, *Phys. Rev. Lett.* **1977**, *39*, 1098.
[12] S. G. Im, K. K. Gleason, E. A. Olivetti, *Appl. Phys. Lett.* **2007**, *90*.
[13] R. M. Howden, E. D. McVay, K. K. Gleason, *J. Mater. Chem. A* **2013**, *1*, 1334.
[14] a) M. C. Barr, J. A. Rowehl, R. R. Lunt, J. Xu, A. Wang, C. M. Boyce, S. G. Im, V. Bulovic, K. K. Gleason, *Adv. Mater.* **2011**, *23*, 3500; b) M. C. Barr, R. M. Howden, R. R. Lunt, V. Bulovic, K. K. Gleason, *Adv. Energy Mater.* **2012**, *2*, 1404.
[15] H. Chelawat, S. Vaddiraju, K. Gleason, *Chem. Mater.* **2010**, *22*, 2864.
[16] K. Kawano, R. Pacios, D. Poplavskyy, J. Nelson, D. D. C. Bradley, J. R. Durrant, *Sol. Energy Mater. Sol. Cells* **2006**, *90*, 3520.
[17] K. Norrman, M. V. Madsen, S. A. Gevorgyan, F. C. Krebs, *J. Am. Chem. Soc.* **2010**, *132*, 16883.
[18] a) J. S. Huang, P. F. Miller, J. S. Wilson, A. J. de Mello, J. C. de Mello, D. D. C. Bradley, *Adv. Funct. Mater.* **2005**, *15*, 290; b) J. Huang, P. F. Miller, J. C. de Mello, A. J. de Mello, D. D. C. Bradley, *Synth. Metals* **2003**, *139*, 569.
[19] E. Vitoratos, S. Sakkopoulos, E. Dalas, N. Paliatsas, D. Karageorgopoulos, F. Petraki, S. Kennou, S. A. Choulis, *Organ. Electron.* **2009**, *10*, 61.
[20] J. P. Lock, S. G. Im, K. K. Gleason, *Macromolecules* **2006**, *39*, 5326.
[21] D. C. Martin, J. Wu, C. M. Shaw, Z. King, S. A. Spanninga, S. Richardson-Burns, J. Hendricks, J. Yang, *Polym. Rev.* **2010**, *50*, 340.
[22] C. J. Powell, A. Jablonski, I. S. Tilinin, S. Tanuma, D. R. Penn, *J. Electron Spectrosc. Related Phenomena* **1999**, *98–99*, 1.
[23] J. F. Moulder, J. Chastain, *Handbook of* X-ray *Photoelectron Spectroscopy: A Reference Book of Standard Spectra for Identification and Interpretation of XPS Data*, Perkin-Elmer Corporatioon, Physical Electronics Division, **1992**.
[24] Y. H. Kim, C. Sachse, M. L. Machala, C. May, L. Muller-Meskamp, K. Leo, *Adv. Funct. Mater.* **2011**, *21*, 1076.
[25] J. Wu, M. Agrawal, H. A. Becerril, Z. Bao, Z. Liu, Y. Chen, P. Peumans, *ACS Nano* **2010**, *4*, 43.
[26] H. A. Becerril, J. Mao, Z. Liu, R. M. Stoltenberg, Z. Bao, Y. Chen, *ACS Nano* **2008**, *2*, 463.
[27] C. Feng, K. Liu, J.-S. Wu, L. Liu, J.-S. Cheng, Y. Zhang, Y. Sun, Q. Li, S. Fan, K. Jiang, *Adv. Funct. Mater.* **2010**, *20*, 885.
[28] a) D. C. Paine, T. Whitson, D. Janiac, R. Beresford, C. O. Yang, B. Lewis, *J. Appl. Phys.* **1999**, *85*, 8445; b) B. G. Lewis, D. C. Paine, *MRS Bull.* **2000**, *25*, 22; c) H. Kim, C. M. Gilmore, A. Piqué, J. S. Horwitz, H. Mattoussi, H. Murata, Z. H. Kafafi, D. B. Chrisey, *J. Appl. Phys.* **1999**, *86*, 6451; d) R. G. Gordon, *MRS Bull.* **2000**, *25*, 52.
[29] B. L. Groenendaal, F. Jonas, D. Freitag, H. Pielartzik, J. R. Reynolds, *Adv. Mater.* **2000**, *12*, 481.
[30] D. M. DeLongchamp, B. D. Vogt, C. M. Brooks, K. Kano, J. Obrzut, C. A. Richter, O. A. Kirillov, E. K. Lin, *Langmuir* **2005**, *21*, 11480.
[31] a) E. F. Schubert, *Light-Emitting Diodes*, SPIE – The International Society for Optical Engineering, **2002**; b) J. Tauc, *Amorphous and Liquid Semiconductors*, Plenum Press, London and New York **1974**.
[32] a) F. L. Xue, Y. Su, K. Varahramyan, *IEEE Trans. Electron. Dev.* **2005**, *52*, 1982; b) P. Rannou, M. Nechtschein, *Synth. Metals* **1999**, *101*, 474.
[33] J. K. Lee, J. M. Cho, W. S. Shin, S. J. Moon, N. T. Kemp, H. Zhang, R. Lamb, *J. Korean Phys. Soc.* **2008**, *52*, 621.
[34] a) B. Zimmermann, U. Wurfel, M. Niggemann, *Sol. Energy Mater. Sol. Cells* **2009**, *93*, 491; b) A. M. Nardes, M. Kemerink, M. M. de Kok, E. Vinken, K. Maturova, R. A. J. Janssen, *Organ. Electron.* **2008**, *9*, 727; c) A. M. Nardes, M. Kemerink, R. A. J. Janssen, J. A. M. Bastiaansen, N. M. M. Kiggen, B. M. W. Langeveld, A. van Breemen, M. M. de Kok, *Adv. Mater.* **2007**, *19*, 1196.
[35] I. Winter, C. Reese, J. Hormes, G. Heywang, F. Jonas, *Chem. Phys.* **1995**, *194*, 207.
[36] Y. Shigesato, D. C. Paine, T. E. Haynes, *Jpn. J. Appl. Phys. Lett.* **1993**, *32*, L1352.
[37] a) M. R. Abidian, D. C. Martin, *Biomaterials* **2008**, *29*, 1273; b) D. K. Taggart, Y. Yang, S.-C. Kung, T. M. McIntire, R. M. Penner, *Nano Lett.* **2011**, *11*, 125.
[38] S. Kirchmeyer, K. Reuter, *J. Mater. Chem.* **2005**, *15*, 2077.
[39] a) J. Lee, S. Lee, G. Li, M. A. Petruska, D. C. Paine, S. Sun, *J. Am. Chem. Soc.* **2012**, *134*, 13410; b) S. Lee, D. C. Paine, *Appl. Phys. Lett.* **2013**, *102*, 052101.